

# Statistical Properties of three-dimensional Hall Magnetohydrodynamics Turbulence

Sharad K Yadav<sup>1,\*</sup>, Hideaki Miura<sup>2,†</sup> and Rahul Pandit<sup>1,‡</sup>

<sup>1</sup> Centre for Condensed Matter Theory, Department of Physics,  
Indian Institute of Science (IISc.), Bangalore 560012, India and

<sup>2</sup> National Institute for Fusion Science (NIFS), Toki, Gifu 509-5292, Japan

(Dated: May 31, 2021)

The three-dimensional (3D) Hall magnetohydrodynamics (HMHD) equations are often used to study turbulence in the solar wind. Some earlier studies have investigated the statistical properties of 3D HMHD turbulence by using simple shell models or pseudospectral direct numerical simulations (DNSs) of the 3D HMHD equations; these DNSs have been restricted to modest spatial resolutions and have covered a limited parameter range. To explore the dependence of 3D HMHD turbulence on the Reynolds number  $Re$  and the ion-inertial scale  $d_i$ , we have carried out detailed pseudospectral DNSs of the 3D HMHD equations and their counterparts for 3D MHD ( $d_i = 0$ ). We present several statistical properties of 3D HMHD turbulence, which we compare with 3D MHD turbulence by calculating (a) the temporal evolution of the energy-dissipation rates and the energy, (b) the wave-number dependence of fluid and magnetic spectra, (c) the probability distribution functions (PDFs) of the cosines of the angles between various pairs of vectors, such as the velocity and the magnetic field, and (d) various measures of the intermittency in 3D HMHD and 3D MHD turbulence.

## I. INTRODUCTION

Electrically conducting fluids can exhibit turbulence that is characterised not only by fluctuations in the fluid velocity and the vorticity, but also in the magnetic field and the current. At the simplest level, such fluids can be modelled by using the equations of magnetohydrodynamics (MHD) [1–9]. Examples of such conducting-fluid flows can be found in liquid metals, in the interiors of planets or in laboratories [10–13], in solar or stellar settings [1–4], in the solar wind [14–19], and in the interstellar medium [1–4, 20]. The MHD description of a plasma is based on a single-fluid approximation. However, in plasmas like the solar wind, this single-fluid assumption is not valid, especially at small scales comparable to or smaller than the ion-inertial length scale  $d_i = c/\omega_{pi}$ , with  $c$  the velocity of light and the ion plasma frequency  $\omega_{pi} \equiv \sqrt{4\pi n_i Z^2 e^2/m_i}$ , where  $Z$  is the charge state,  $n_i$  the ion density, and  $m_i$  the mass of the ion. Hall magnetohydrodynamics (HMHD) is a simplified fluid description of a plasma that accounts for two-fluid effects, to some extent; HMHD includes the Hall term in Ohm's law [21–44]; and it reduces to MHD if  $d_i = 0$ . Shell models have also been developed to study the statistical properties of HMHD turbulence [38, 45]. The HMHD partial differential equations (PDEs) pose several challenges for mathematicians, who study the regularity properties of solutions of these PDEs [46, 47], for fluid dynamicists and statistical mechanicians, who seek to characterise the statistical properties of HMHD turbulence, and for astrophysicists, who use these PDEs to model turbulence in

astrophysical systems such as the solar wind. The solar wind [2, 14–17, 48–56] has been described as a turbulence laboratory [50], for it is in a highly turbulent state: the magnetic Reynolds number  $Re_M$  lies in the range  $10^5 \lesssim Re_M \lesssim 10^9$  and the magnetic Prandtl number  $Pr_M \simeq 1$ ; the kinetic- and magnetic-energy spectra,  $E_u(k)$  and  $E_b(k)$ , respectively, extend over many decades of the wave number  $k$ ; for time-domain measurements,  $k$  is replaced by the frequency  $f$ . Satellite observations of solar-wind-plasma turbulence [15, 52–59] have shown that, in the inertial range,  $E_u(f) \sim f^{-\alpha}$ , with  $\alpha \simeq 5/3$ , the scaling exponent that follows from the Kolmogorov hypotheses [60] of 1941 (henceforth K41). In contrast, the magnetic-energy spectrum has two different scaling or inertial ranges (henceforth, we refer to them as the *inertial* and *intermediate-dissipation* ranges): (i) for  $f_I \ll f \ll f_{ci}$ ,  $E_b(f) \sim f^{-\alpha}$ , where the frequency  $f_I$  is related inversely to the integral length scale of the turbulence,  $f_{ci}$ , the ion-cyclotron frequency, is related inversely to  $d_i$  and  $\alpha \simeq 5/3$  is consistent with the K41 value; (ii) for  $f_{ci} \ll f \ll f_d$ , where the frequency  $f_d$  is related inversely to the dissipation length scale at which viscous losses become significant,  $E_b(f) \sim f^{-\alpha_1}$ , with  $\alpha_1$  in the range of  $1 \lesssim \alpha_1 \lesssim 4$ . The solar wind is unlike a well-controlled experiments in a laboratory, so it is not surprising that spectral exponents show a range of values (see, e.g., Ref. [61], Fig. 5 in Ref. [62], and Fig. 3 of Ref. [56]); this variability of exponents has been attributed to transients, unsteady conditions, anisotropies, and effects that lie beyond an incompressible-MHD description [62]. Solar-wind-turbulence data have also been analysed to uncover (a) intermittency and multiscaling of velocity and magnetic-field structure functions [52, 63] and (b) the alignment of velocity and magnetic-field fluctuations [16]. In particular, the study of Ref. [52] has found structure-function multiscaling (simple scaling), in the first (second) frequency range mentioned above. The magnetosheath is another near-Earth space plasma; for a

\* sharadyadav@iisc.ac.in; Current address: Department of Physics, Sardar Vallabhbhai National Institute of Technology (SVNIT), Surat 395007, India.

† miura.hideaki@nifs.ac.jp

‡ rahul@iisc.ac.in; Also at Jawaharlal Nehru Centre for Advanced Scientific Research (JNCASR), Jakkur, Bangalore, India.

comparison of plasma turbulence in the solar wind and in the magnetosheath we refer the reader to Refs. [56, 59].

There has been a steady stream of theoretical studies and direct numerical simulations (DNSs) of HMHD [21–44]; most of these concentrate on three-dimensional (3D) HMHD or related shell-model or large-eddy-simulation investigations. These studies yield a spectral exponent  $\alpha \simeq 5/3$ , which is consistent with K41; however, the values of the spectral exponent  $\alpha_1$ , suggested in different theoretical and DNS studies, lie in a large range:  $1 \lesssim \alpha_1 \lesssim 5.5$ ; clearly, it is more challenging to develop an understanding of 3D HMHD turbulence than of its MHD and fluid counterparts. Some of these works (see, e.g., Refs. [33, 37, 39, 43]) have provided phenomenological arguments for the values of  $\alpha_1$  that have been obtained in different DNSs. It has been suggested that, in addition to  $d_i$  and the Reynolds and Prandtl numbers, the statistical properties of 3D HMHD might well depend on other parameters like the Alfvén number, which is the ratio of kinetic and magnetic energies. Furthermore, DNSs have explored (a) the intermittency and multiscaling of velocity and magnetic-field structure functions [30, 38, 54, 63, 64] and (b) the alignment of velocity and magnetic-field fluctuations [16].

Given the uncertainties in spectral exponents and the statistical properties of 3D HMHD turbulence, it behooves us to initiate systematic investigations of these properties of the type that have been carried out for 3D MHD turbulence [8, 65]. We present such a study. In particular, we use extensive pseudospectral DNSs, with two different types of initial conditions [henceforth, the initial conditions A and B (see below)], to obtain the statistical properties of turbulence in the unforced 3D HMHD equations; a comparison of such properties provides valuable insights into the initial-condition dependence of the exponent  $\alpha_1$  and multiscaling exponents. Before we present the details of our work, we provide a qualitative overview of the principal results from our DNSs:

- **Spectra:** In our 3D MHD and 3D HMHD DNSs, in the inertial range mentioned above, both

$$\begin{aligned} E_u(k) &\sim k^{-\alpha}; \\ E_b(k) &\sim k^{-\alpha}; \end{aligned} \quad (1)$$

the value of the spectral exponent  $\alpha$  consistent with the K41 result  $5/3$ . In the intermediate-dissipation range, with lengths  $l$  in the range  $d_i \ll l \ll \eta_d^b$ , where  $\eta_d^b$  is the magnetic-dissipation length scale,

$$E_b(k) \sim k^{-\alpha_1}, \quad (2)$$

with the value of  $\alpha_1$  is consistent with (A)  $11/3$ , for the initial condition A, and (B)  $7/3$ , for the initial condition B (see Sec. II for precise definitions of these spectra and the initial conditions). We also explore the  $k$ -dependence of other spectra and of the wave-number-dependent Alfvén number  $E_b(k)/E_u(k)$  for these two initial conditions.

- **Probability distribution functions (PDFs):**

- We compute the PDFs of the cosines of the angles between various fields, such as the velocity  $\mathbf{u}$ , vorticity  $\boldsymbol{\omega} = \nabla \times \mathbf{u}$ , magnetic field  $\mathbf{b}$ , and current density  $\mathbf{j} = \nabla \times \mathbf{b}$ , to highlight the importance of the Hall term in suppressing the tendency of alignment (or antialignment) of these fields for both the initial conditions (A) and (B).
- We also explore intermittency in 3D HMHD turbulence (and compare it with its 3D MHD counterpart) by calculating the PDFs of the velocity and magnetic-field increments as a function of the separation length scale  $l$ . We find evidence of small-scale intermittency in our 3D HMHD plasma turbulence DNSs (as in 3D MHD plasma turbulence DNSs); our DNSs, especially those for the initial condition (A), show clearly that intermittency is suppressed significantly in the second scaling range of 3D HMHD plasma turbulence, in agreement with the results of solar-wind measurements [52].

- **Structure functions:** We compute the  $l$ -dependence of velocity and magnetic-field structure functions and, therefrom, their order- $p$  multiscaling exponents  $\zeta_p^u$  and  $\zeta_p^b$ , respectively. In the inertial range,  $\zeta_p^u$  and  $\zeta_p^b$  are nonlinear, monotone increasing functions of  $p$ ; this is a clear signature of multiscaling. By contrast, in the intermediate-dissipation range,  $\zeta_p^u$  and  $\zeta_p^b$  increase linearly with  $p$ , a hallmark of simple scaling; this linear dependence is in consonance with solar-wind results [52].

The remainder of this paper is organized as follows. In Sec. II we present the 3D HMHD PDEs (Subsection II A), the pseudospectral DNSs we employ to solve these PDEs, and the definitions of various statistical measures (Subsection II B) that we use to characterise 3D HMHD turbulence. In Sec. III we provide results from our DNSs in three subsections: In Subsection III A we discuss the temporal evolution of the energy-dissipation rates and the energy and the wave-number dependence of spectra, such as  $E_u(k)$  and  $E_b(k)$ . In Subsection III B we compute PDFs of the cosines of the angles between the following pairs of vectors:  $\{\mathbf{u}, \mathbf{b}\}$ ,  $\{\mathbf{u}, \mathbf{j}\}$ ,  $\{\mathbf{u}, \boldsymbol{\omega}\}$ ,  $\{\mathbf{b}, \mathbf{j}\}$ ,  $\{\mathbf{b}, \boldsymbol{\omega}\}$ , and  $\{\boldsymbol{\omega}, \mathbf{j}\}$ ; by using these PDFs we quantify the degree of alignment between these pairs of vectors. In Subsection III C we characterise intermittency in 3D HMHD turbulence by examining the  $l$  dependence PDFs of velocity- and magnetic-field increments and of the order- $p$  structure functions of these increments. Finally, we discuss the implications of our study in Sec. IV. In the Appendix we present some joint PDFs.

## II. MODEL AND METHODS

We begin with the 3D HMHD PDEs (Subsection II A); then we present an outline of our pseudospectral DNS method and the definitions of statistical measures (Subsection II B) for 3D HMHD turbulence.

### A. Basic Equations

Three-dimensional (3D) HMHD is described by the following set of coupled PDEs for  $\mathbf{u}$  and  $\mathbf{b}$ :

$$\frac{\partial \mathbf{u}}{\partial t} + (\mathbf{u} \cdot \nabla) \mathbf{u} = -\nabla \bar{p} + (\mathbf{b} \cdot \nabla) \mathbf{b} + \nu \nabla^2 \mathbf{u} + \mathbf{f}_{\mathbf{u}}; \quad (3)$$

$$\frac{\partial \mathbf{b}}{\partial t} = \nabla \times (\mathbf{u} \times \mathbf{b} - d_i \mathbf{j} \times \mathbf{b}) + \eta \nabla^2 \mathbf{b} + \mathbf{f}_{\mathbf{b}}; \quad (4)$$

$$\nabla \cdot \mathbf{u} = 0; \nabla \cdot \mathbf{b} = 0. \quad (5)$$

Equation (3) is the momentum equation; this includes a contribution from the Lorentz force  $\mathbf{j} \times \mathbf{b}$ , with the current density  $\mathbf{j} = \nabla \times \mathbf{b}$ , which can be separated into the magnetic-tension term  $(\mathbf{b} \cdot \nabla) \mathbf{b}$  and the magnetic pressure, which we combine with the pressure  $p$  to obtain the total pressure  $\bar{p} \equiv p + |\mathbf{b}|^2/4\pi$ . The induction equation (4) uses the generalized form of Ohm's law, which includes the Hall term  $\sim \mathbf{j} \times \mathbf{b}$ , whose coefficient  $d_i$  is the ion-inertial length;  $\eta$  and  $\nu$  are, respectively, the kinematic viscosity and the magnetic resistivity (or diffusivity);  $\mathbf{f}_{\mathbf{u}}$  and  $\mathbf{f}_{\mathbf{b}}$  are the forcing terms. The Poisson equation for  $\bar{p}$  follows from the divergence of Eq. (3) and the incompressibility condition  $\nabla \cdot \mathbf{u} = 0$ :

$$\nabla^2 \bar{p} = \nabla \cdot [(\mathbf{b} \cdot \nabla) \mathbf{b} - (\mathbf{u} \cdot \nabla) \mathbf{u}] + \nabla \cdot \mathbf{f}_{\mathbf{u}} \quad (6)$$

We study decaying HMHD turbulence, so we set  $\mathbf{f}_{\mathbf{u}} = 0$  and  $\mathbf{f}_{\mathbf{b}} = 0$ . Thus, the final form for the pressure-Poisson equation is

$$\nabla^2 \bar{p} = \nabla \cdot [(\mathbf{b} \cdot \nabla) \mathbf{b} - (\mathbf{u} \cdot \nabla) \mathbf{u}]. \quad (7)$$

### B. Direct Numerical Simulations and Statistical Measures

We solve Eqs. (3) and (4) by using the pseudospectral method in a cubical domain of side  $L = 2\pi$ , with periodic boundary conditions (see, e.g., Ref. [8] for 3D MHD). We remove the aliasing error, because of the nonlinear terms, by using the 2/3 dealiasing method. For time integration we employ the second-order slaved, Adams-Bashforth scheme.

We perform four sets of simulations, *Run1*, *Run2*, *Run3*, and *Run4*, in which the initial energy spectra (initial condition A) for the velocity and magnetic fields are as follows:

$$E_u^0(k) = E_b^0(k) = E^0 k^4 \exp(-2k^2), \quad (8)$$

where  $E^0 \simeq 10$  is the initial amplitude in our DNSs. For the DNSs *Run5a*, *Run5b*, and *Run5c* these initial spectra (initial condition B) are

$$E_u^0(k) = E_b^0(k) = E^0 k^2 \exp(-2k^2). \quad (9)$$

The phases of the Fourier modes of the velocity and magnetic fields in Eqs. 8 and 9 are distributed randomly and uniformly on the interval  $[0, 2\pi)$ . Some data from the DNSs *Run5a*, *Run5b*, and *Run5c* have been published [34], in a different context; we carry out a detailed comparison of results from *Run1-Run4* and *Run5a-Run5c*. The values of various parameters from our DNSs are listed in Table I.

To characterize the statistical properties of 3D MHD and 3D HMHD turbulence, we compute the following (cf. Ref. [8] for 3D MHD turbulence):

- At time  $t$  we obtain the kinetic-energy, magnetic-energy, kinetic-energy-dissipation-rate, magnetic-energy-dissipation-rate, and pressure spectra, which are, respectively:

$$\begin{aligned} E_u(k, t) &\equiv \sum_{k-\frac{1}{2} \leq k' \leq k+\frac{1}{2}} |\tilde{\mathbf{u}}(\mathbf{k}', t)|^2; \\ E_b(k, t) &\equiv \sum_{k-\frac{1}{2} \leq k' \leq k+\frac{1}{2}} |\tilde{\mathbf{b}}(\mathbf{k}', t)|^2; \\ \epsilon_u(k, t) &= \nu k^2 E_u(k, t); \\ \epsilon_b(k, t) &= \eta k^2 E_b(k, t); \\ P(k, t) &\equiv \sum_{k-\frac{1}{2} \leq k' \leq k+\frac{1}{2}} |\tilde{\bar{p}}(\mathbf{k}', t)|^2; \end{aligned} \quad (10)$$

here, tildes denote spatial Fourier transforms, and  $k' \equiv |\mathbf{k}'|$ ; we compute the time evolution of different energies and dissipation rates by summing the corresponding spectrum over the wave number  $k$ ; e.g.,  $E_u(t) = \sum_k E_u(k, t)$ . In the inertial and intermediate-dissipation ranges mentioned above, these spectra show power-law dependences on  $k$ , which we elucidate below.

- We compute PDFs of the cosine of the angles between the following pairs of vectors, to characterise the degree of alignment between them:  $\{\mathbf{u}, \mathbf{b}\}$ ,  $\{\mathbf{u}, \mathbf{j}\}$ ,  $\{\mathbf{u}, \omega\}$ ,  $\{\mathbf{b}, \mathbf{j}\}$ ,  $\{\mathbf{b}, \omega\}$ , and  $\{\omega, \mathbf{j}\}$ .
- To characterise multifractality and the intermittency we calculate the order- $p$ , equal-time longitudinal structure functions at time  $t$ :

$$\begin{aligned} S_p^a(l) &= \langle |\delta a_{\parallel}(\mathbf{x}, l)|^p \rangle; \\ \delta a_{\parallel}(\mathbf{a}, l) &= [\mathbf{a}(\mathbf{x} + \mathbf{l}, t) - \mathbf{a}(\mathbf{x}, t) \cdot \frac{\mathbf{l}}{l}]; \end{aligned} \quad (11)$$

here,  $\mathbf{a}_{\parallel}$  is the longitudinal component of  $\mathbf{a}$ , which is  $\mathbf{u}$  or  $\mathbf{b}$  for velocity and magnetic-field structure functions and  $\delta a_{\parallel}(\mathbf{a}, l)$  the longitudinal component

<i>Run</i>	$N$	$\nu$	$Pr_M$	$d_i$	$\delta t$	$u_{rms}$	$l_I$	$\lambda$	$Re_\lambda$	$t_c$	$k_{max}\eta_d^u$	$k_{max}\eta_d^b$
<i>Run1</i>	256	$10^{-3}$	1	0.0	$5.0 \times 10^{-4}$	0.29	1.193	0.13	39	6.76	2.09	1.89
<i>Run2</i>	256	$10^{-3}$	1	0.05	$5.0 \times 10^{-4}$	0.13	0.12	0.128	17	7.4	2.1	1.8
<i>Run3</i>	512	$5.0 \times 10^{-4}$	1	0.0	$10^{-4}$	0.28	0.29	0.25	142	9.13	1.82	1.65
<i>Run4</i>	512	$5.0 \times 10^{-4}$	1	0.05	$10^{-4}$	0.29	0.32	0.28	165	9.65	1.8	1.6
<i>Run5a</i>	1024	$5.0 \times 10^{-4}$	1	0.0	$10^{-4}$	1.0	0.35	0.07	143	0.5	1.53	1.37
<i>Run5b</i>	1024	$5.0 \times 10^{-4}$	1	0.025	$10^{-4}$	1.0	0.37	0.08	153	0.5	1.60	1.30
<i>Run5c</i>	1024	$5.0 \times 10^{-4}$	1	0.05	$10^{-4}$	1.0	0.36	0.09	176	0.5	1.71	1.25

TABLE I. *Parameters in our DNSs Run1, Run2, Run3, Run4, Run5a, Run5b, and Run5c*:  $N^3$  is the number of collocation points;  $\nu$  is the kinematic viscosity;  $Pr_M$  is the magnetic Prandtl number;  $d_i$  is the ion-inertial length (it is 0 for the MHD runs);  $\delta t$  is the time step;  $u_{rms}$ ,  $l_I$ ,  $\lambda$ , and  $Re_\lambda$  are the root-mean-square velocity, the integral scale, the Taylor microscale, and the Taylor-microscale Reynolds number, respectively. Most of these quantities are obtained at the cascade-completion time  $t_c$  (see text);  $\eta_d^u$  and  $\eta_d^b$  are, respectively, the Kolmogorov dissipation length scales for the velocity and magnetic fields.  $k_{max}$  is the magnitude of the largest wave numbers in our DNSs ( $k_{max} \simeq 85.33, 170.67, \text{ and } 343.33$  for  $N = 256, 512, \text{ and } 1024$ , respectively).

of its increment; we suppress  $t$  in the arguments of structure functions for notational convenience. In the inertial range

$$\begin{aligned} S_p^u(l) &\sim l^{\zeta_p^u}; \\ S_p^b(l) &\sim l^{\zeta_p^b}; \end{aligned} \quad (12)$$

$\zeta_p^u$  and  $\zeta_p^b$  are the velocity and magnetic-field multiscaling exponents of order  $p$ . As we show below, in 3D HMHD turbulence, the magnetic-field spectra and structure functions exhibit two different scaling regions called *inertial* and *intermediate-dissipation* regions; e.g.,

$$\begin{aligned} d_i \ll l \ll L; S_p^b(l) &\sim l^{\zeta_p^{b,1}}; \\ \eta_d^b \ll l \ll d_i; S_p^b(l) &\sim l^{\zeta_p^{b,2}}; \end{aligned} \quad (13)$$

here,  $\zeta_p^{b,1}$  and  $\zeta_p^{b,2}$  are the multiscaling exponents in these two scaling regions. To study intermittency we also compute PDFs of velocity and magnetic field increments and the hyperflatnesses

$$F_6^a(l) = S_6^a(l)/[S_2^a(l)]^3. \quad (14)$$

### III. RESULTS

We present the results of our DNSs in three subsections: In Subsection III A we discuss the temporal evolution of the energy-dissipation rates and the energy; we then present the spectra that we have defined above. In Subsection III B we compute probability distribution functions (PDFs) of the cosine of the angles between the following pairs of vectors:  $\{\mathbf{u}, \mathbf{b}\}$ ,  $\{\mathbf{u}, \mathbf{j}\}$ ,  $\{\mathbf{u}, \boldsymbol{\omega}\}$ ,  $\{\mathbf{b}, \mathbf{j}\}$ ,  $\{\mathbf{b}, \boldsymbol{\omega}\}$ , and  $\{\boldsymbol{\omega}, \mathbf{j}\}$ ; these PDFs help us to quantify the

degree of alignment between these pairs. In Subsection III C we characterise intermittency in 3D HMHD turbulence by examining PDFs of velocity and magnetic-field increments and the  $l$  dependences of order- $p$  structure functions of these increments.

#### A. Temporal Evolution and Spectra

In Fig. 1(a) we display the time evolution of the kinetic-energy dissipation rate (blue curves), the magnetic-energy dissipation rate (red curves), and total-energy dissipation rate (black curves) from *Run1* (dashed lines) and *Run2* (solid lines) for 3D MHD and 3D HMHD turbulence, respectively. We remark that these dissipation rates increase sharply, up until a cascade-completion time  $\tau_c$ , and then they decay slowly. The peak positions are nearly the same for all these curves; the peaks for *Run1* occur marginally earlier than they do in *Run2*. In Fig. 1(b) we present the time dependence of the fluid, magnetic, and total energies in simulations *Run1* and *Run2*. Figures 1(c) and 1(d) are the counterparts of Figs. 1(a) and 1(b) for *Run3* and *Run4*. Figures 1(e) and 1(f) display the spectra of the kinetic-energy-dissipation rate and the magnetic energy-dissipation rate, respectively, at  $\tau_c$  for *Run1*, *Run2*, *Run3*, *Run4*, *Run5a*, *Run5b*, and *Run5c*; the well-developed peaks in these spectra show that our DNSs are well resolved; we also summarise this in Table I, which shows that  $k_{max}\eta_d^u > 1$  and  $k_{max}\eta_d^b > 1$  for all these runs.

In Fig. 2 we show the compensated spectra of the kinetic energy and the magnetic energy  $E_u(k)$  (open circles)  $E_b(k)$  (asterisks), respectively, which we have obtained from our DNSs at the cascade-completion time  $\tau_c$ . Specifically, we present log-log (base 10) plots versus the wave number  $k$  of the following: (a)  $k^{5/3}E_u(k)$

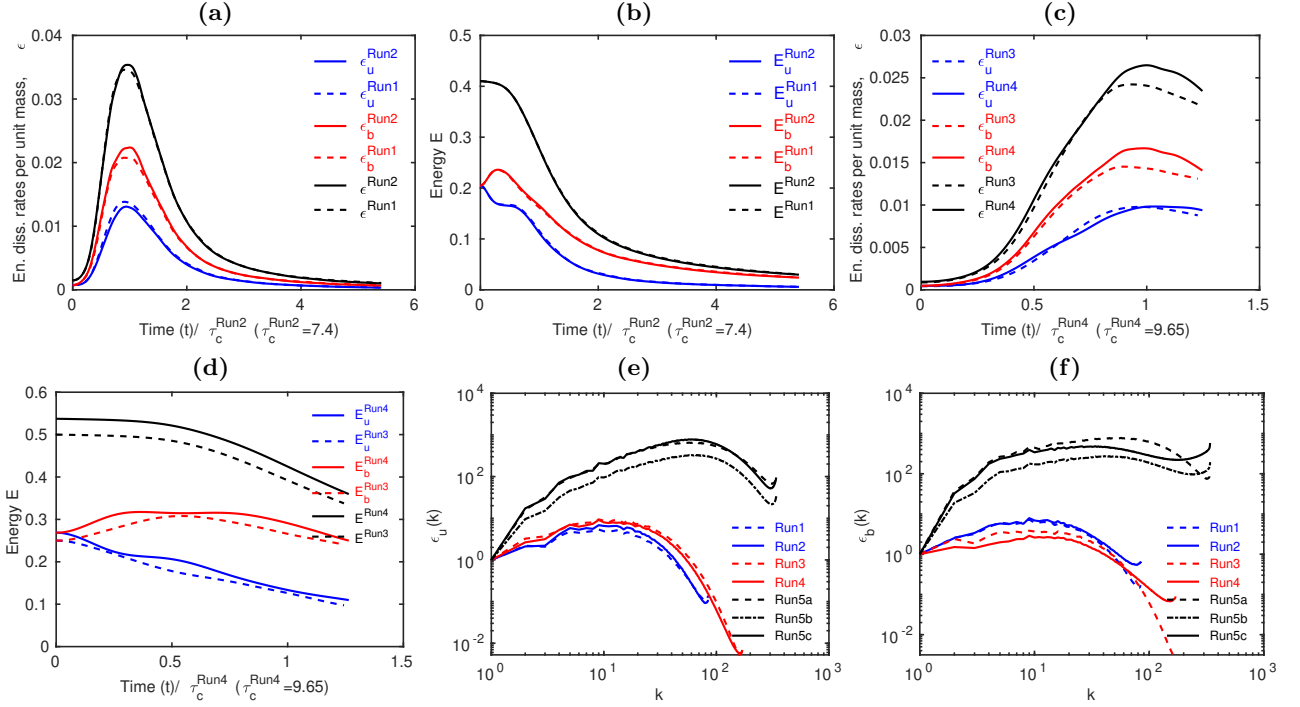


FIG. 1. (Color online) Plots versus the scaled time  $t$  of (a) the kinetic-energy dissipation rate  $\epsilon_u$  (blue curves), magnetic-energy dissipation rate  $\epsilon_b$  (red curves), and the total-energy dissipation rate  $\epsilon$  (black curves) for *Run1* (dashed lines) and *Run2* (solid lines); and (b) the kinetic energy  $E_u$  (blue curve), magnetic energy  $E_b$  (red curve), and the total energy  $E$  (black curve) for *Run1* (dashed lines) and *Run2* (solid lines). (c) and (d) are, respectively, the counterparts of (a) and (b) for *Run3* and *Run4*. Log-log (base 10) plots versus the wave number  $k$  of (e) the kinetic-energy-dissipation-rate spectra  $\epsilon_u(k)$  and (f) the magnetic-energy-dissipation-rate spectra  $\epsilon_b(k)$  from *Run1* (dashed-blue curve), *Run2* (solid-blue curve), *Run3* (dashed-red curve), *Run4* (solid-red curve), *Run5a* (dashed-black curve), *Run5b* (dashed-dot black curve), and *Run5c* (solid-black curve).

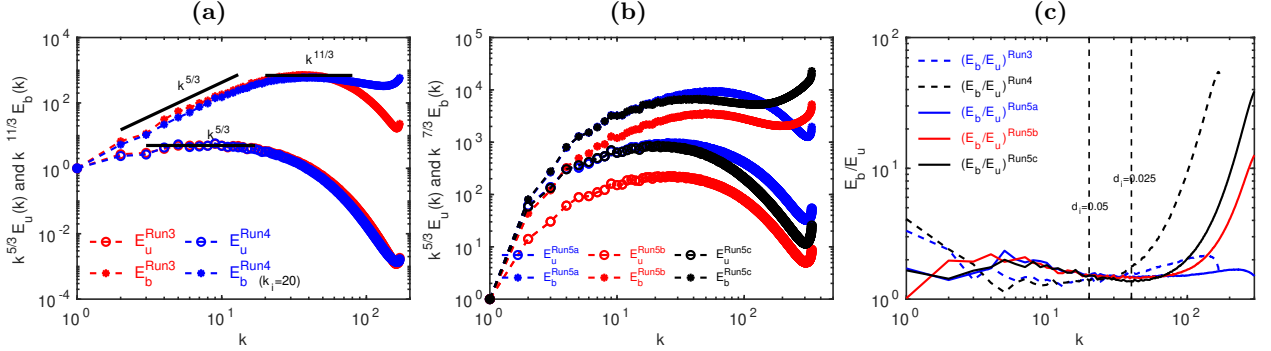


FIG. 2. Log-log (base 10) plots versus the wave number  $k$  of: (a) the compensated kinetic energy spectra  $k^{5/3}E_u(k)$  (lower two curves) and the compensated magnetic energy spectra  $k^{11/3}E_b(k)$  (upper two curves) from *Run3* (red curves) and *Run4* (blue curves); solid black lines indicate different power-law regions; (b) the compensated kinetic energy spectra  $k^{5/3}E_u(k)$  (lower three curves) and the compensated magnetic energy spectra  $k^{7/3}E_b(k)$  (upper three curves) from *Run5a* (blue curves), *Run5b* (red curves), and *Run5c* (black curves); solid black lines indicate different power-law regions; (c) the wave-number-dependent Alfvén ratios  $(E_b(k)/E_u(k))$  for *Run3*, *Run4*, *Run5a*, *Run5b* and *Run5c*. We compute these spectra at the cascade-completion time  $\tau_c$ ; and the wavenumber  $k_i \propto 1/d_i$ .

(lower two curves) and  $k^{11/3}E_b(k)$  (upper two curves) from *Run3* (red curves) and *Run4* (blue curves), with solid black lines indicating different power-law regions (Fig. 2(a)); (b)  $k^{5/3}E_u(k)$  (lower three curves) and the compensated magnetic energy spectra  $k^{11/3}E_b(k)$  (upper three curves) from *Run5a* (blue curves), *Run5b* (red

curves), and *Run5c* (black curves); (c) the wave-number-dependent Alfvén ratios  $E_b(k)/E_u(k)$  for *Run3*, *Run4*, *Run5a*, *Run5b* and *Run5c* (Fig. 2(c)); the wavenumber  $k_i \propto 1/d_i$ . From these plots we conclude that the spectral

exponents (Eqs. 1 and 2) are consistent with

$$\begin{aligned}\alpha &\simeq 5/3, & \text{the K41 value;} \\ \alpha_1 &\simeq 11/3, & \text{for initial condition A;} \\ \alpha_1 &\simeq 7/3, & \text{for initial condition B.}\end{aligned}\quad (15)$$

The values of  $\alpha_1$  are clearly different for initial condition A (Eq. 8 and *Run2* & *Run4*) and initial condition B (Eq. 9 and *Run5b* – *Run5c*). These differences stem, in part, from the disparities in the wave-number-dependent Alfvén ratios  $E_b(k)/E_u(k)$  (Fig. 2(c)) and, as we show in Subsection III B, in the alignment PDFs of various vector fields. In all our runs, the ratio  $E_b(k)/E_u(k)$  lies in the range 1 – 2 at small values of  $k \lesssim k_i \propto d_i$ ; for  $k_i < k < k_{max}$  this ratio is different for different runs. For example, for *Run5c*,  $E_b(k)/E_u(k)$  remains nearly constant up until  $k \sim 60$ , i.e., for almost three decades beyond  $k_i$ ; by contrast, for *Run4* this ratio rises rapidly, with increasing  $k$ , at large  $k$ . For *Run5c*, this near constancy, with  $E_b(k)/E_u(k)$  in the range 1 – 2, indicates approximate equipartition of the energies in the velocity and magnetic fields. It has been recognised [39] that such equipartition suggests  $\alpha_1 = 7/3$ . In contrast,  $\alpha_1 = 11/3$  can be obtained by equating  $\tau_{nl}$  and  $\tau_h$  and by using  $E_b/E_u = d_i^2 k^2$ , where  $\tau_{nl}$  is the energy-transfer because of the nonlinear term in the momentum equation and  $\tau_h$  is the energy-transfer time because of the Hall term in the induction equation [39].

## B. Probability Distribution Functions

In Fig. 3 we display, at the cascade-completion time  $\tau_c$ , the PDFs of the cosine of the angles between the following pairs of vectors:  $\{\mathbf{u}, \mathbf{b}\}$ ,  $\{\mathbf{u}, \mathbf{j}\}$ ,  $\{\mathbf{u}, \boldsymbol{\omega}\}$ ,  $\{\mathbf{b}, \mathbf{j}\}$ ,  $\{\mathbf{b}, \boldsymbol{\omega}\}$  and  $\{\boldsymbol{\omega}, \mathbf{j}\}$ , for *Run3* (blue curve) and *Run4* (red curve). We present their counterparts for *Run5a* (blue curve), *Run5b* (red curve) and *Run5c* (black curve) in Fig. 4. In Figs. 3 and 4 the blue curves are from the MHD runs *Run3* and *Run5a* (see Table I).

In all these PDFs, there are, roughly speaking, two peaks at  $\cos\theta \simeq \pm 1$ , which quantify the degree of antialignment ( $\theta = 180^\circ$ ) and of alignment ( $\theta = 0^\circ$ ) between the two vectors. The amplitudes of these peaks depend upon the parameters in our DNSs. One qualitative trend shows up clearly: the alignment and antialignment peaks (Figs. 3(a) and 4(a) for the pair  $\{\mathbf{u}, \mathbf{b}\}$ ) are more pronounced in the 3D MHD runs (*Run3* and *Run5a*) than in their 3D HMHD counterparts; and this peak-suppression trend appears in most of the PDFs we show in Figs. 3 and 4. In 3D MHD, the alignment or antialignment of  $\{\mathbf{u}, \mathbf{b}\}$  is associated with a *depletion of nonlinearity*. This can be seen most simply by writing the 3D MHD equations in terms of Elsässer variables [9]. To the extent that the alignment or antialignment peaks in the PDF of the cosine of the angle between  $\{\mathbf{u}, \mathbf{b}\}$  are suppressed in 3D HMHD, relative to 3D MHD, we conclude that this depletion of nonlinearity is also suppressed.

We remark that the PDFs of the cosines of the angles mentioned above are related to PDFs of various helicities, which we list below:

$$\begin{aligned}H_c &= \langle \mathbf{u} \cdot \mathbf{b} \rangle; \\ H_m &= \langle \mathbf{a} \cdot \mathbf{b} \rangle; \\ H_u &= \langle \mathbf{u} \cdot \boldsymbol{\omega} \rangle; \\ H_g &= H_m + 2d_i H_c + d_i^2 H_u.\end{aligned}\quad (16)$$

Here,  $H_c$  is the cross helicity;  $H_m$  is the magnetic helicity, with  $\mathbf{a}$  the vector potential that follows from  $\mathbf{b} = \nabla \times \mathbf{a}$ ;  $H_u$  is the kinetic helicity; and  $H_g$  is a generalised helicity that is useful in 3D HMHD.  $H_u$  is conserved for an ideal, unforced fluid; in the absence of forcing,  $H_m$  is conserved in both ideal 3D MHD and ideal 3D HMHD;  $H_c$  is conserved in ideal, unforced 3D MHD, but not in its 3D HMHD counterpart; in ideal, unforced 3D HMHD the generalised cross helicity  $H_g$  is conserved [66].

It is useful to define the electron velocity  $\mathbf{v}_e \equiv \mathbf{u} - d_i \nabla \times \mathbf{b}$  [29]. In Figs. 6(a) and 6(b) we present, respectively, the PDFs of the cosines of the angles between (a)  $\mathbf{v}_e$  and  $\mathbf{j}$  and (b)  $\mathbf{v}_e$  and  $\mathbf{b}$  from runs *Run5a* (blue curve), *Run5b* (red curve), and *Run5c* (black curve). In Figs. 6(c) and 6(d), we present similar plots for *Run3* (blue curve) and *Run4* (red curve).

In the Appendix we present some joint PDFs.

## C. Intermittency

At the cascade completion time  $\tau_c$ , we investigate intermittency in 3D HMHD turbulence, and in its 3D MHD counterpart, by calculating the length-scale- $l$  dependence of (a) PDFs of the velocity and magnetic-field increments (Eq. 11) and (b) of the velocity and magnetic-field structure functions (Eq. 11) and, therefrom, their order- $p$  multiscaling exponents, Eqs. 12 and 13, in the inertial and the intermediate-dissipation ranges. We also examine the dependence on  $l$  of the hyperflatness Eq. 14.

In Figs. 6 and 7 we display the  $l$  dependence of the PDFs of, respectively, the velocity- and magnetic-field increments, from *Run3*, *Run4*, *Run5a*, *Run5b*, and *Run5c*. In these PDFs,  $l$  goes from the the intermediate-dissipation range to the inertial-range:  $l = 0.05$  (blue-solid curves),  $l = 0.11$  (red-dotted curves),  $l = 0.53$  (green dashed-dot curves) and  $l = 3.08$  (magenta dashed curves) from *Run3* and *Run4*; we give similar plots for *Run5a*, *Run5b*, and *Run5c* in Fig. 7; we include, for reference, Gaussian PDFs (black lines) with zero mean and unit variance. We note that the field-increment PDFs show tails that deviate significantly from those of Gaussian PDFs: the smaller the value of  $l$ , the greater this deviation, a clear signature of small-scale intermittency (see, e.g., Ref. [67]).

We turn now to structure functions (Eq. 11), multiscaling exponents (Eqs. 12-13), and the ratios of these exponents. We present plots of such structure functions

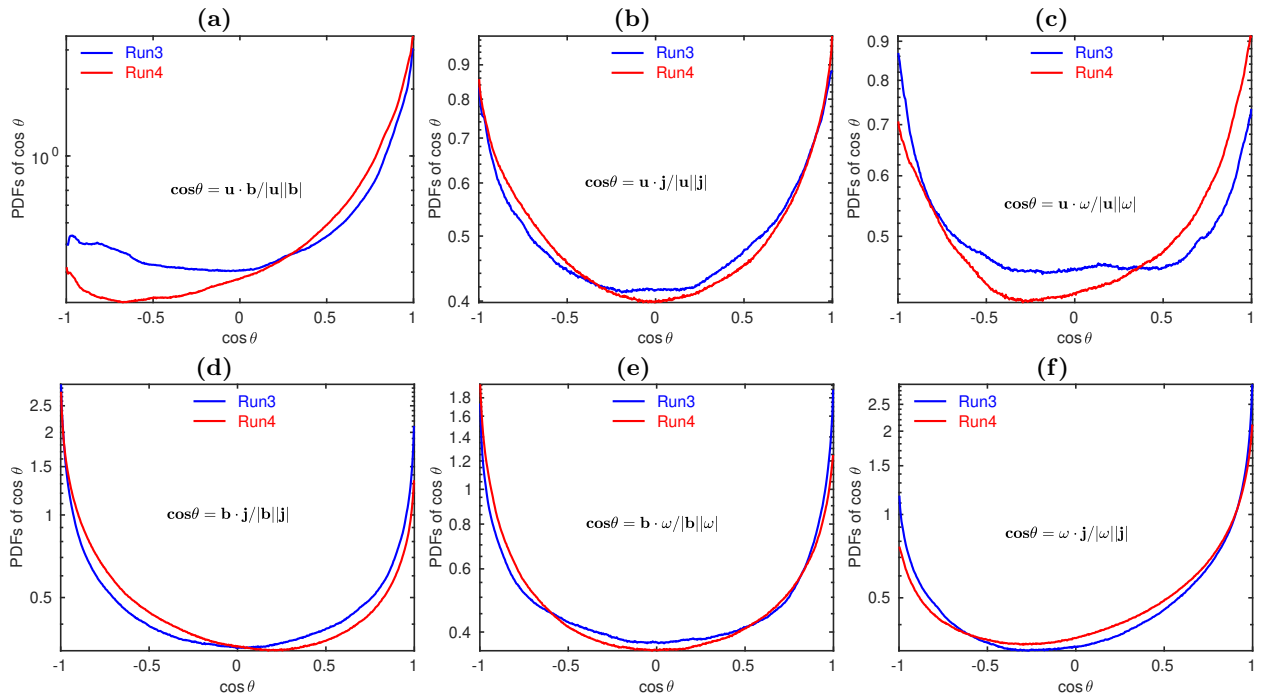


FIG. 3. Semilog (base 10) plots of PDFs of cosines of angles, denoted by  $\theta$ , between (a)  $\mathbf{u}$  and  $\mathbf{b}$ , (b)  $\mathbf{u}$  and  $\mathbf{j}$ , (c)  $\mathbf{u}$  and  $\omega$ , (d)  $\mathbf{b}$  and  $\mathbf{j}$ , (e)  $\mathbf{b}$  and  $\omega$ , and (f)  $\omega$  and  $\mathbf{j}$  from *Run3* (blue curves) and *Run4* (red curves).

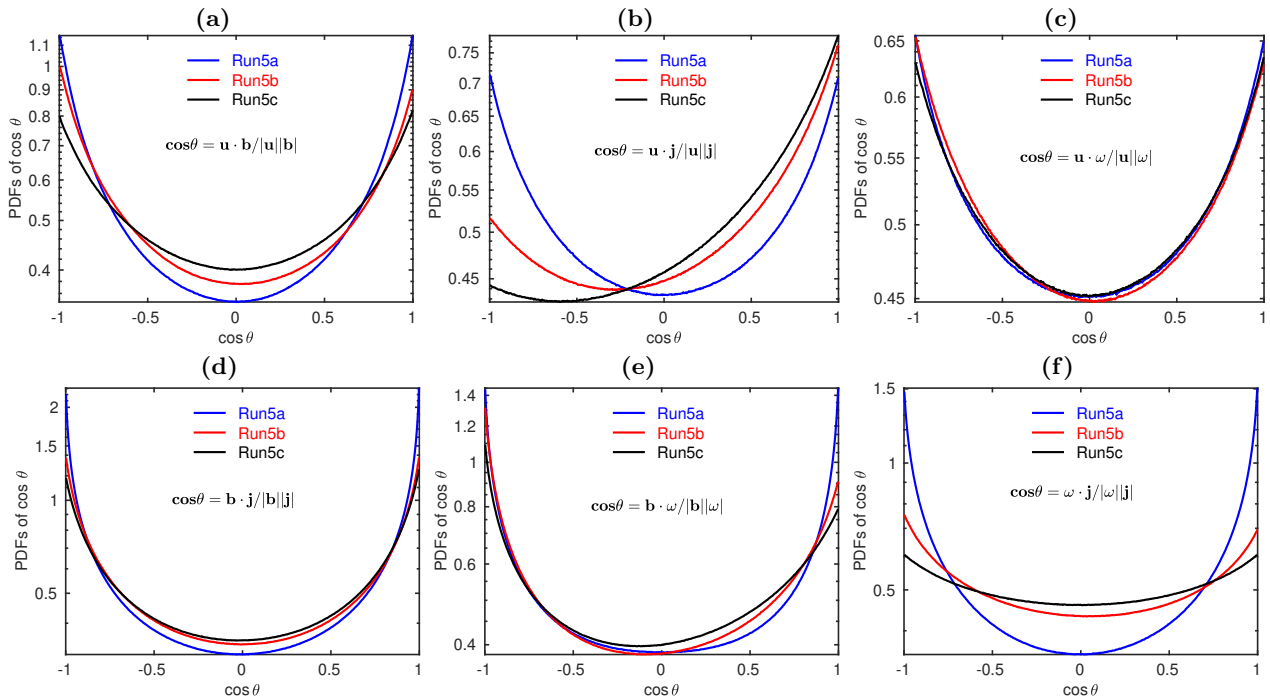


FIG. 4. Semilog (base 10) plots of PDFs of cosines of angles, denoted by  $\theta$ , between (a)  $\mathbf{u}$  and  $\mathbf{b}$ , (b)  $\mathbf{u}$  and  $\mathbf{j}$ , (c)  $\mathbf{u}$  and  $\omega$ , (d)  $\mathbf{b}$  and  $\mathbf{j}$ , (e)  $\mathbf{b}$  and  $\omega$ , and (f)  $\omega$  and  $\mathbf{j}$  from *Run5a* (blue curves), *Run5b* (red curves) and *Run5c* (black curves).

in Figs. 8-12. To extract multiscaling exponents (Eqs. 12-13) directly, we use log-log (base 10) plots of structure functions (Eq. 11) versus the separation  $l$ . We obtain such plots, at  $t_c$ , for *Run3* and *Run4* in, respectively, Figs. 8(a)-(b) and Figs. 9(a)-(b), for order  $p$  from 1 – 6;

we indicate by straight, black lines the regions that we use to obtain estimates for the multiscaling exponents (Eqs. 12-13); we get these exponents and their error bars by using a local-slope analysis [8]. We present plots, versus  $p$ , of the resulting multiscaling exponents (Eqs. 12-

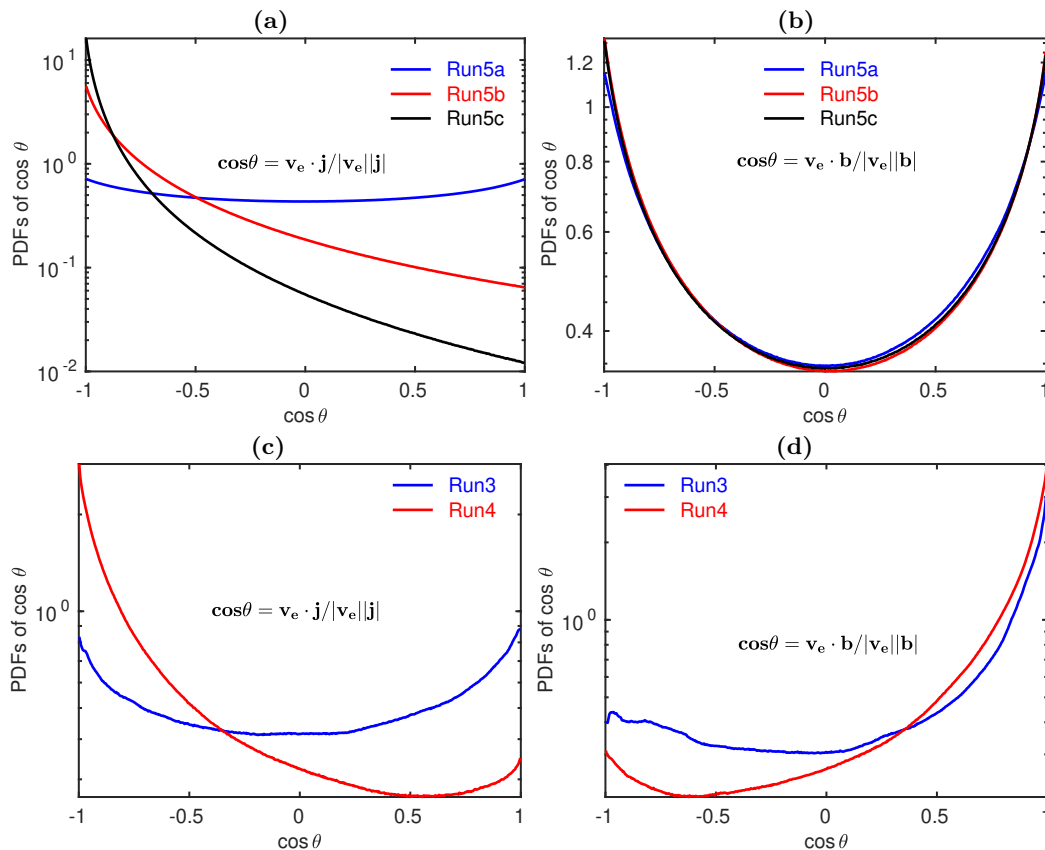


FIG. 5. Semilog (base 10) plots of PDFs of cosines of angles, denoted by  $\theta$ , between (a)  $\mathbf{v}_e$  and  $\mathbf{j}$ , and (b)  $\mathbf{v}_e$  and  $\mathbf{b}$  from *Run5a* (blue curves), *Run5b* (red curves) and *Run5c* (black curves); (c) and (d) are the similar plots from *Run3* (blue curves) and *Run4* (red curves).

13), for *Run3* and *Run4* in, respectively, Figs. 8(c) and Figs. 9(c)-(d). If the scaling range extends over a limited range of scales, this range can often be extended by using the extended-self-similarity (ESS) procedure [68, 69]. In this procedure, we use log-log (base 10) plots of the structure function of order  $p$ , versus, e.g., the  $p = 3$  structure function; straight-line regions in such plots yield the ratios of the order  $p$  and order  $p = 3$  multiscaling exponents (Eqs. 12-13). [This has proved to be especially useful in incompressible-fluid turbulence, where the third-order exponent is known to be 1.] We give such ESS plots for structure functions in Figs. 10(a)-(b) (*Run5a*), Figs. 11(a)-(b) (*Run5b*), and Figs. 12(a)-(b) (*Run5c*); we then plot the resulting multiscaling-exponent (Eqs. 12-13) ratios in Figs. 9(e)-(f) (*Run4*), Fig. 10(c) (*Run5a*), Figs. 11(c)-(d) (*Run5b*), and Figs. 12(c)-(d) (*Run5c*). We list our values for multiscaling exponents (Eqs. 12-13), along with error bars, in Tables II-IV; these Tables provide a quantitative summary of our results for these exponents. We note, at the qualitative level, that prior experimental studies suggest that the magnetic-field structure functions in 3D HMHD turbulence exhibit (a) *inertial* and *intermediate-dissipation* scaling regions and (b) multiscaling is replaced by simple scaling in the second of these ranges; our results are in consonance with these

observations.

The length-scale dependence of the hyperflatness (Eq. 14) is often used to characterise small-scale intermittency. We present semilog plots of the hyperflatnesses (Eq. 14), for the velocity and the magnetic fields, in *Run5a*, *Run5b*, and *Run5c* Figs. 13 (a), (b), and (c), respectively. In these plots, we observe that these hyperflatnesses are more-or-less flat, over a large range of  $l$ , but they increase rapidly, at small  $l$ ; this is the hallmark of small-scale intermittency.

#### IV. CONCLUSIONS

Our study, which has been motivated by the uncertainties in spectral exponents and the statistical properties of 3D HMHD turbulence, is a systematic investigation of these properties by pseudospectral DNSs. Although many numerical studies of 3D HMHD turbulence have been carried out earlier, none of them has compared results from two different types of initial conditions (initial condition A (Eq. 8 and *Run2* – *Run4*) and initial condition B (Eq. 9 and *Run5b* – *Run5c*)) nor studied, in one work, the different statistical properties we consider. (For similar studies of 3D MHD turbulence we refer the reader

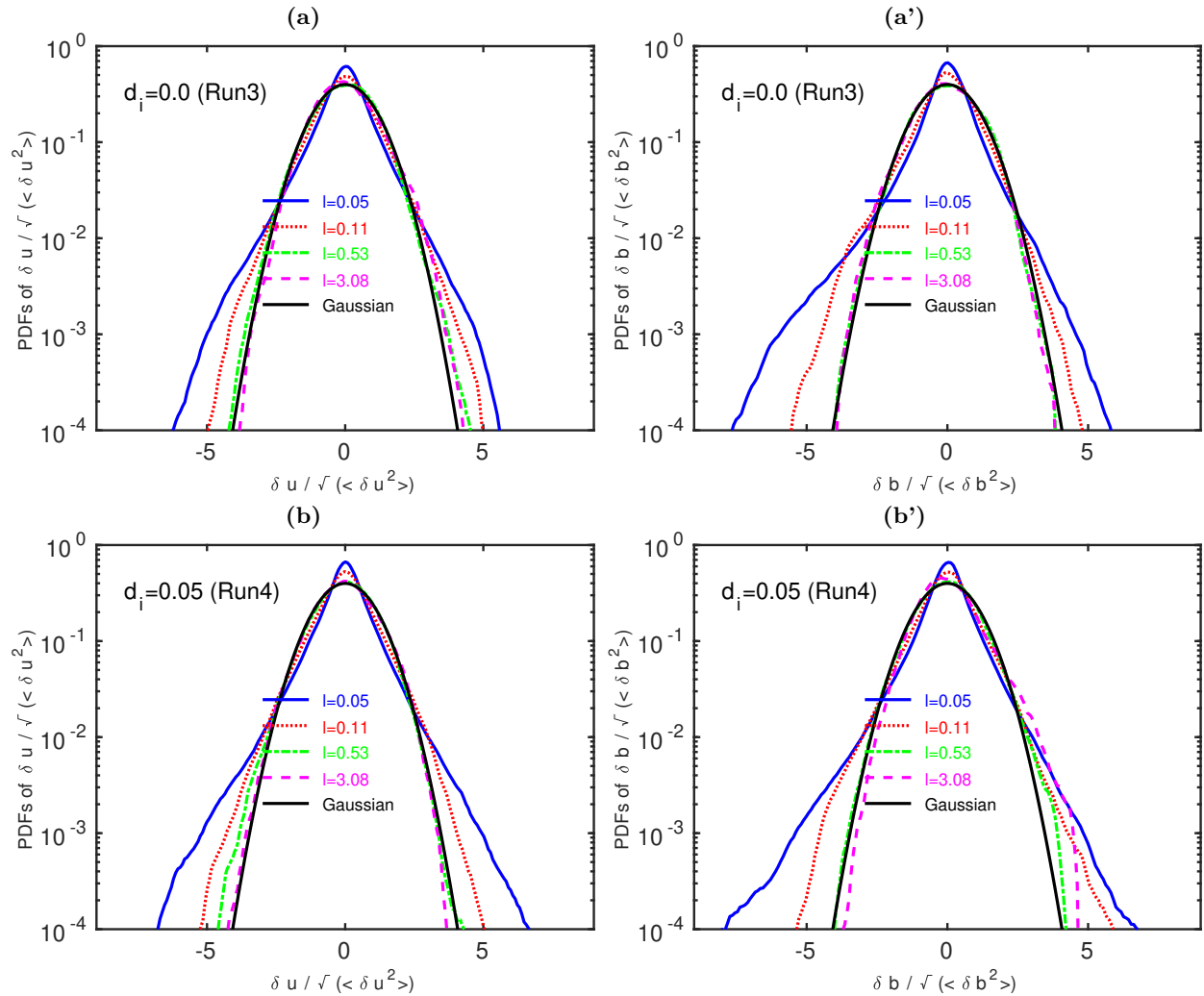


FIG. 6. Semilog (base 10) plots of PDFs of the velocity- (first column) and magnetic-field (second column) increments from *Run3* (first row) and *Run4* (second row) for  $l = 0.05$  (blue solid lines),  $0.11$  (red dotted lines),  $0.53$  (green dashed-dot lines) and  $3.08$  (magenta dashed lines); for reference, we also show zero-mean and unit-variance Gaussian PDFs (black lines).

to Refs. [8, 65]. Our work provides valuable insights into the initial-condition dependence of the spectral exponent  $\alpha_1$  and the multiscaling exponents (Eqs. 12-13). We find clear evidence of inertial- and intermediate-dissipation range scaling, with the value of the spectral exponent  $\alpha$  consistent with the K41 result  $5/3$ . In the intermediate-dissipation range, the value of  $\alpha_1$  is consistent with (A)  $11/3$ , for the initial condition A, and (B)  $7/3$ , for the initial condition B. These different values can be attributed, in part, to the disparities in the  $k$  dependence of  $E_b(k)/E_u(k)$  for these two initial conditions. Our computations of the PDFs of the cosines of the angles between various fields, such as the velocity  $\mathbf{u}$  and  $\boldsymbol{\omega}$  or  $\mathbf{b}$  and  $\mathbf{j}$ , help us to highlight the importance of the Hall term in suppressing the tendency of alignment (or antialignment) of these fields for both the initial conditions (A) and (B). We carry out a careful exploration of intermittency in 3D HMHD turbulence by calculating the PDFs of the velocity and magnetic-field increments as a function of the

separation length scale  $l$ . We compute the  $l$ -dependence of velocity and magnetic-field structure functions and, therefrom, their order- $p$  multiscaling exponents (Eqs. 12-13). In the inertial (intermediate-dissipation) range, we find clear signatures of multiscaling (simple scaling), in consonance with solar-wind results [52].

## ACKNOWLEDGMENTS

RP and SKY thank Nadia Bihari Padhan for discussions. SKY thanks the UGC-D.S. Kothari Postdoctoral Fellowship; RP and SKY thank CSIR and DST (India) for support and SERC (IISc) for computational resources. This research was partially supported by JSPS KAKENHI Grant Number 17K05734 and 20H00225, Japan. The numerical simulations were performed on *Plasma Simulator* of NIFS with the support and under the auspices of the NIFS Collaboration Research pro-

$p$	$\zeta_p^{u,Run3}$	$\zeta_p^{b,Run3}$	$\zeta_p^{u,Run4}$	$\zeta_p^{(b,1),Run4}$	$\zeta_p^{(b,2),Run4}$
1	$0.35 \pm 0.06$	$0.45 \pm 0.03$	$0.34 \pm 0.04$	$0.40 \pm 0.04$	$0.71 \pm 0.06$
2	$0.65 \pm 0.10$	$0.81 \pm 0.07$	$0.64 \pm 0.07$	$0.76 \pm 0.10$	$1.31 \pm 0.13$
3	$0.90 \pm 0.13$	$1.09 \pm 0.12$	$0.90 \pm 0.06$	$1.08 \pm 0.18$	$1.83 \pm 0.16$
4	$1.13 \pm 0.17$	$1.32 \pm 0.15$	$1.14 \pm 0.12$	$1.34 \pm 0.28$	$2.28 \pm 0.21$
5	$1.35 \pm 0.22$	$1.53 \pm 0.17$	$1.36 \pm 0.32$	$1.49 \pm 0.38$	$2.69 \pm 0.39$
6	$1.58 \pm 0.28$	$1.73 \pm 0.18$	$1.57 \pm 0.66$	$1.53 \pm 0.50$	$3.10 \pm 0.70$

TABLE II. List of the multiscaling exponents (Eqs. 12-13), for *Run3* and *Run4*. *Run4* has two sets of exponents, one for the inertial range and the other for the intermediate-dissipation range (see text).

$p$	$(\zeta_p^u/\zeta_3^u)^{Run3}$	$(\zeta_p^b/\zeta_3^b)^{Run3}$	$(\zeta_p^u/\zeta_3^u)^{Run4}$	$(\zeta_p^{b,1}/\zeta_3^{b,1})^{Run4}$	$(\zeta_p^{b,2}/\zeta_3^{b,2})^{Run4}$
1	$0.39 \pm 0.01$	$0.42 \pm 0.01$	$0.38 \pm 0.03$	$0.38 \pm 0.04$	$0.39 \pm 0.02$
2	$0.72 \pm 0.01$	$0.75 \pm 0.01$	$0.71 \pm 0.04$	$0.71 \pm 0.04$	$0.72 \pm 0.03$
3	$1.0 \pm 0.00$	$1.0 \pm 0.00$	$1.0 \pm 0.00$	$1.0 \pm 0.00$	$1.0 \pm 0.00$
4	$1.27 \pm 0.01$	$1.22 \pm 0.02$	$1.26 \pm 0.13$	$1.23 \pm 0.05$	$1.25 \pm 0.08$
5	$1.54 \pm 0.02$	$1.42 \pm 0.04$	$1.52 \pm 0.36$	$1.37 \pm 0.12$	$1.48 \pm 0.22$
6	$1.82 \pm 0.04$	$1.61 \pm 0.07$	$1.76 \pm 0.72$	$1.39 \pm 0.24$	$1.71 \pm 0.39$

TABLE III. List of the ratios of multiscaling exponents (Eqs. 12-13), for *Run3* and *Run4*. *Run4* has two sets of exponents, one for the inertial range and the other for the intermediate-dissipation range (see text).

gram(NIFS20KNSSS133), as well as on the Oakforest-PACS supercomputer of the University of Tokyo, being partially supported by the Joint Usage/Research Center for Interdisciplinary Large-Scale Information Infrastructures in Japan (jh190006-NAJ, jh200002-NAH).

### Appendix: Joint Probability Distribution Functions

We display color-contour-plots of the joint probability distribution functions (JPDFs) of  $Q$  and  $R$ , at the cascade-completion time  $\tau_c$ , in Fig. 14 from *Run3*, *Run4*, *Run5a* and *Run5c*, with  $Q$  and  $R$  the following, well-known invariants (see, e.g., Ref. [8]) for an ideal, incompressible fluid:

$$\begin{aligned} Q &= -\frac{1}{2}tr(A^2); \\ R &= -\frac{1}{3}tr(A^3); \end{aligned} \quad (A.1)$$

here,  $A$  is the velocity-derivative tensor with components  $A_{ij} = \partial_i u_j$ ; the zero-discriminant line  $D = \frac{27}{4}R^2 + Q^3 =$

0 is shown by black curves in these plots. We observe that the characteristic, tear-drop shape of these JPDFs of  $Q$  and  $R$  are more prominent in 3D HMHD turbulence (*Run4* and *Run5c*) than in their 3D MHD counterparts (*Run3* and *Run5a*); and the tails of these JPDFs are more elongated in 3D HMHD turbulence (*Run4* and *Run5c*) than in their 3D MHD counterparts (*Run3* and *Run5a*).

In Fig. 15 we show plots of JPDFs of  $\omega$  and  $j$ , the moduli of the vorticity and the current, at the cascade-completion time  $\tau_c$ , from *Run3*, *Run4*, *Run5a* and *Run5c*. We observe that in 3D MHD turbulence (*Run3* and *Run5a*) the outer region of the JPDFs of  $\omega$  and  $j$  show curved, roughly circular, contours, whereas in 3D HMHD turbulence (*Run4* and *Run5c*) the counterparts of these contours are flattened and suppressed significantly; furthermore, there is an elongation of the JPDFs of  $\omega$  and  $j$  along the axes, at low values of  $\omega$  and  $j$ .

[1] A. R. Choudhuri *et al.*, *The physics of fluids and plasmas: an introduction for astrophysicists* (Cambridge Univer-

sity Press, 1998).

$p$	$(\zeta_p^u/\zeta_3^u)_{Run5a}$	$(\zeta_p^b/\zeta_3^b)_{Run5a}$	$(\zeta_p^u/\zeta_3^u)_{Run5b}$	$(\zeta_p^{b,1}/\zeta_3^{b,1})_{Run5b}$	$(\zeta_p^{b,2}/\zeta_3^{b,2})_{Run5b}$	$(\zeta_p^u/\zeta_3^u)_{Run5c}$	$(\zeta_p^{b,1}/\zeta_3^{b,1})_{Run5c}$	$(\zeta_p^{b,2}/\zeta_3^{b,2})_{Run5c}$
1	$0.39 \pm 0.01$	$0.40 \pm 0.01$	$0.36 \pm 0.01$	$0.35 \pm 0.01$	$0.35 \pm 0.01$	$0.36 \pm 0.01$	$0.35 \pm 0.01$	$0.34 \pm 0.01$
2	$0.73 \pm 0.01$	$0.73 \pm 0.01$	$0.70 \pm 0.02$	$0.69 \pm 0.01$	$0.68 \pm 0.01$	$0.69 \pm 0.01$	$0.69 \pm 0.01$	$0.67 \pm 0.01$
3	$1.0 \pm 0.00$	$1.0 \pm 0.00$	$1.0 \pm 0.00$	$1.0 \pm 0.00$	$1.0 \pm 0.00$	$1.0 \pm 0.00$	$1.0 \pm 0.00$	$1.0 \pm 0.00$
4	$1.21 \pm 0.02$	$1.21 \pm 0.02$	$1.28 \pm 0.04$	$1.29 \pm 0.02$	$1.30 \pm 0.01$	$1.28 \pm 0.03$	$1.29 \pm 0.03$	$1.32 \pm 0.01$
5	$1.36 \pm 0.05$	$1.39 \pm 0.06$	$1.55 \pm 0.12$	$1.55 \pm 0.04$	$1.60 \pm 0.04$	$1.52 \pm 0.10$	$1.56 \pm 0.08$	$1.65 \pm 0.04$
6	$1.47 \pm 0.10$	$1.54 \pm 0.11$	$1.81 \pm 0.23$	$1.79 \pm 0.09$	$1.89 \pm 0.08$	$1.73 \pm 0.20$	$1.80 \pm 0.17$	$1.99 \pm 0.09$

TABLE IV. List of the ratios of multiscaling exponents (Eqs. 12-13), obtained via the ESS procedure (see text), for *Run5a*, *Run5b*, and *Run5c*. *Run5b* and *Run5c* have two sets of exponents, one for the inertial range and the other for the intermediate-dissipation range (see text).

- [2] V. Krishan, *Astrophysical plasmas and fluids*, Vol. 235 (Springer Science & Business Media, 1999).
- [3] G. Rüdiger and R. Hollerbach, *The magnetic universe: geophysical and astrophysical dynamo theory* (John Wiley & Sons, 2006).
- [4] J. H. Goedbloed, J. Goedbloed, and S. Poedts, *Principles of magnetohydrodynamics: with applications to laboratory and astrophysical plasmas* (Cambridge university press, 2004).
- [5] D. Biskamp, *Magnetohydrodynamic turbulence* (Cambridge University Press, 2003).
- [6] M. K. Verma, Statistical theory of magnetohydrodynamic turbulence: recent results, *Physics Reports* **401**, 229 (2004).
- [7] P. A. Davidson, *An introduction to magnetohydrodynamics* (2002).
- [8] G. Sahoo, P. Perlekar, and R. Pandit, Systematics of the magnetic-prandtl-number dependence of homogeneous, isotropic magnetohydrodynamic turbulence, *New Journal of Physics* **13**, 013036 (2011).
- [9] A. Basu, A. Naji, and R. Pandit, Structure-function hierarchies and von kármán–howarth relations for turbulence in magnetohydrodynamical equations, *Physical Review E* **89**, 012117 (2014).
- [10] K. Moffatt and E. Dormy, *Self-exciting fluid dynamos*, Vol. 59 (Cambridge University Press, 2019).
- [11] P. H. Roberts and G. A. Glatzmaier, Geodynamo theory and simulations, *Reviews of modern physics* **72**, 1081 (2000).
- [12] W. L. Shew and D. P. Lathrop, Liquid sodium model of geophysical core convection, *Physics of the Earth and Planetary Interiors* **153**, 136 (2005).
- [13] R. Monchaux, M. Berhanu, M. Bourgoïn, M. Moulin, P. Odier, J.-F. Pinton, R. Volk, S. Fauve, N. Mordant, F. Pétrélis, *et al.*, Generation of a magnetic field by dynamo action in a turbulent flow of liquid sodium, *Physical review letters* **98**, 044502 (2007).
- [14] C. Salem, A. Mangeney, S. Bale, and P. Veltri, Solar wind magnetohydrodynamics turbulence: anomalous scaling and role of intermittency, *The Astrophysical Journal* **702**, 537 (2009).
- [15] J. Podesta, D. Roberts, and M. Goldstein, Spectral exponents of kinetic and magnetic energy spectra in solar wind turbulence, *The Astrophysical Journal* **664**, 543 (2007).
- [16] J. Podesta, B. D. Chandran, A. Bhattacharjee, D. Roberts, and M. Goldstein, Scale-dependent angle of alignment between velocity and magnetic field fluctuations in solar wind turbulence, *Journal of Geophysical Research: Space Physics* **114** (2009).
- [17] J. M. Weygand, W. Matthaeus, S. Dasso, M. Kivelson, and R. Walker, Taylor scale and effective magnetic reynolds number determination from plasma sheet and solar wind magnetic field fluctuations, *Journal of Geophysical Research: Space Physics* **112** (2007).
- [18] A. Pouquet, D. Rosenberg, and J. E. Stawarz, Interplay between turbulence and waves: large-scale helical transfer, and small-scale dissipation and mixing in fluid and hall-mhd turbulence, *Rendiconti Lincei. Scienze Fisiche e Naturali* **31**, 949 (2020).
- [19] A. Pouquet, J. E. Stawarz, and D. Rosenberg, Coupling large eddies and waves in turbulence: Case study of magnetic helicity at the ion inertial scale, *Atmosphere* **11**, 203 (2020).
- [20] D. Falceta-Gonçalves, G. Kowal, E. Falgarone, and A.-L. Chian, Turbulence in the interstellar medium, *Nonlinear Processes in Geophysics* **21**, 587 (2014).
- [21] M. J. Lighthill, Studies on magneto-hydrodynamic waves and other anisotropic wave motions, *Philosophical Transactions of the Royal Society of London. Series A, Mathematical and Physical Sciences* **252**, 397 (1960).
- [22] D. O. Gómez, P. D. Mininni, and P. Dmitruk, Hall-magnetohydrodynamic small-scale dynamos, *Physical Review E* **82**, 036406 (2010).
- [23] B. Hnat, S. C. Chapman, and G. Rowlands, Compressibility in solar wind plasma turbulence, *Physical review letters* **94**, 204502 (2005).
- [24] T. S. Horbury, M. Forman, and S. Oughton, Anisotropic scaling of magnetohydrodynamic turbulence, *Physical Review Letters* **101**, 175005 (2008).
- [25] L. N. Martin, P. Dmitruk, and D. O. Gomez, Energy spectrum, dissipation, and spatial structures in reduced hall magnetohydrodynamic, *Physics of Plasmas* **19**, 052305 (2012).
- [26] P. D. Mininni, D. O. Gómez, and S. M. Mahajan, Dynamo action in hall magnetohydrodynamics, *The Astrophysical Journal Letters* **567**, L81 (2002).
- [27] P. D. Mininni, D. O. Gómez, and S. M. Mahajan, Dynamo action in magnetohydrodynamics and hall-magnetohydrodynamics, *The Astrophysical Journal* **587**, 472 (2003).
- [28] P. D. Mininni, D. O. Gómez, and S. M. Mahajan, Direct simulations of helical hall-mhd turbulence and dynamo action, *The Astrophysical Journal* **619**, 1019 (2005).
- [29] P. D. Mininni, A. Alexakis, and A. Pouquet, Energy transfer in hall-mhd turbulence: cascades, backscatter,

- and dynamo action, *Journal of plasma physics* **73**, 377 (2007).
- [30] G. Boffetta, A. Celani, A. Crisanti, and R. Prandi, Intermittency of two-dimensional decaying electron magnetohydrodynamic turbulence, *Physical Review E* **59**, 3724 (1999).
- [31] S. Chapman, B. Hnat, and K. Kiyani, Solar cycle dependence of scaling in solar wind fluctuations, *Nonlinear Processes in Geophysics* **15**, 445 (2008).
- [32] D. Shaikh and P. Shukla, 3d simulations of fluctuation spectra in the hall-mhd plasma, *Physical Review Letters* **102**, 045004 (2009).
- [33] D. Hori and H. Miura, Spectrum properties of hall mhd turbulence, *Plasma and Fusion Research* **3**, S1053 (2008).
- [34] H. Miura and K. Araki, Structure transitions induced by the hall term in homogeneous and isotropic magnetohydrodynamic turbulence, *Physics of Plasmas* **21**, 072313 (2014).
- [35] H. Miura, K. Araki, and F. Hamba, Hall effects and sub-grid-scale modeling in magnetohydrodynamic turbulence simulations, *Journal of Computational Physics* **316**, 385 (2016).
- [36] H. Miura and K. Araki, Coarse-graining study of homogeneous and isotropic hall magnetohydrodynamics turbulence, *Plasma Physics and Controlled Fusion* **55**, 014012 (2012).
- [37] H. Miura, J. Yang, and T. Gotoh, Hall magnetohydrodynamic turbulence with a magnetic prandtl number larger than unity, *Physical Review E* **100**, 063207 (2019).
- [38] D. Banerjee, S. S. Ray, G. Sahoo, and R. Pandit, Multiscaling in hall-magnetohydrodynamic turbulence: insights from a shell model, *Physical review letters* **111**, 174501 (2013).
- [39] S. Galtier and E. Buchlin, Multiscale hall-magnetohydrodynamic turbulence in the solar wind, *The Astrophysical Journal* **656**, 560 (2007).
- [40] S. Galtier, von kármán–howarth equations for hall magnetohydrodynamic flows, *Physical Review E* **77**, 015302 (2008).
- [41] R. Meyrand and S. Galtier, Spontaneous chiral symmetry breaking of hall magnetohydrodynamic turbulence, *Physical review letters* **109**, 194501 (2012).
- [42] R. Meyrand, K. H. Kiyani, Ö. D. Gürçan, and S. Galtier, Coexistence of weak and strong wave turbulence in incompressible hall magnetohydrodynamics, *Physical Review X* **8**, 031066 (2018).
- [43] V. Krishan and S. Mahajan, Magnetic fluctuations and hall magnetohydrodynamic turbulence in the solar wind, *Journal of Geophysical Research: Space Physics* **109** (2004).
- [44] D. O. Gómez, P. D. Mininni, and P. Dmitruk, Mhd simulations and astrophysical applications, *Advances in Space Research* **35**, 899 (2005).
- [45] D. Hori, M. Furukawa, S. Ohsaki, and Z. Yoshida, A shell model for the hall mhd system, *Journal of Plasma and Fusion Research* **81**, 141 (2005).
- [46] D. Chae, P. Degond, and J.-G. Liu, Well-posedness for hall-magnetohydrodynamics, in *Annales de l'IHP Analyse non linéaire*, Vol. 31 (2014) pp. 555–565.
- [47] A. Alghamdi, S. Gala, and M. Ragusa, A regularity criterion of smooth solution for the 3d viscous hall-mhd equations, *Aims Mathematics* **3**, 565 (2018).
- [48] M. L. Goldstein, D. Roberts, and W. Matthaeus, Magnetohydrodynamic turbulence in the solar wind, *Annual review of astronomy and astrophysics* **33**, 283 (1995).
- [49] M. K. Verma, Nonclassical viscosity and resistivity of the solar wind plasma, *Journal of Geophysical Research: Space Physics* **101**, 27543 (1996).
- [50] R. Bruno and V. Carbone, The solar wind as a turbulence laboratory, *Living Rev. Sol. Phys.* **10**, 2 (2013).
- [51] R. Bruno and V. Carbone, *Turbulence in the solar wind*, Vol. 928 (Springer, 2016).
- [52] K. Kiyani, S. Chapman, Y. V. Khotyaintsev, M. Dunlop, and F. Sahraoui, Global scale-invariant dissipation in collisionless plasma turbulence, *Physical review letters* **103**, 075006 (2009).
- [53] W. H. Matthaeus and M. L. Goldstein, Measurement of the rugged invariants of magnetohydrodynamic turbulence in the solar wind, *Journal of Geophysical Research: Space Physics* **87**, 6011 (1982).
- [54] W. H. Matthaeus, M. Wan, S. Servidio, A. Greco, K. T. Osman, S. Oughton, and P. Dmitruk, Intermittency, nonlinear dynamics and dissipation in the solar wind and astrophysical plasmas, *Philosophical Transactions of the Royal Society A: Mathematical, Physical and Engineering Sciences* **373**, 20140154 (2015).
- [55] O. Alexandrova, C. H. K. Chen, L. Sorriso-Valvo, T. S. Horbury, and S. D. Bale, Solar wind turbulence and the role of ion instabilities, *Space Science Reviews* **178**, 101 (2013).
- [56] F. Sahraoui, L. Hadid, and S. Huang, Magnetohydrodynamic and kinetic scale turbulence in the near-earth space plasmas: a (short) biased review, *Reviews of Modern Plasma Physics* **4**, 1 (2020).
- [57] O. Alexandrova, V. Carbone, P. Veltri, and L. Sorriso-Valvo, Small-scale energy cascade of the solar wind turbulence, *The Astrophysical Journal* **674**, 1153 (2008).
- [58] O. Alexandrova, V. Carbone, P. Veltri, and L. Sorriso-Valvo, Solar wind cluster observations: Turbulent spectrum and role of hall effect, *Planetary and Space Science* **55**, 2224 (2007).
- [59] G. Zimbardo, A. Greco, L. Sorriso-Valvo, S. Perri, Z. Vörös, G. Aburjania, K. Chargazia, and O. Alexandrova, Magnetic turbulence in the geospace environment, *Space science reviews* **156**, 89 (2010).
- [60] U. Frish, *Turbulence: The legacy of A. N. Kolmogorov* (Cambridge University Press, Cambridge, England, 1995).
- [61] B. J. Vasquez, V. I. Abramenko, D. K. Haggerty, and C. W. Smith, Numerous small magnetic field discontinuities of bartels rotation 2286 and the potential role of alfvénic turbulence, *Journal of Geophysical Research: Space Physics* **112** (2007).
- [62] W. H. Matthaeus, D. C. Montgomery, M. Wan, and S. Servidio, A review of relaxation and structure in some turbulent plasmas: magnetohydrodynamics and related models, *Journal of Turbulence* **13**, N37 (2012).
- [63] M. Wan, K. T. Osman, W. H. Matthaeus, and S. Oughton, Investigation of intermittency in magnetohydrodynamics and solar wind turbulence: scale-dependent kurtosis, *The Astrophysical Journal* **744**, 171 (2011).
- [64] P. Rodriguez Imazio, L. N. Martin, P. Dmitruk, and P. D. Mininni, Intermittency in hall-magnetohydrodynamics with a strong guide field, *Physics of Plasmas* **20**, 052506 (2013).
- [65] V. Dallas and A. Alexakis, Structures and dynamics of small scales in decaying magnetohydrodynamic turbu-

- lence, *Physics of Fluids* **25**, 105106 (2013).
- [66] L. Turner, Hall effects on magnetic relaxation, *IEEE Transactions on Plasma Science* **14**, 849 (1986).
- [67] R. Pandit, P. Perlekar, and S. S. Ray, Statistical properties of turbulence: an overview, *Pramana* **73**, 157 (2009).
- [68] R. Benzi, S. Ciliberto, R. Tripiccone, C. Baudet, F. Masaioli, and S. Succi, Extended self-similarity in turbulent flows, *Physical review E* **48**, R29 (1993).
- [69] S. Chakraborty, U. Frisch, and S. S. Ray, Extended self-similarity works for the burgers equation and why, *Journal of fluid mechanics* **649**, 275 (2010).

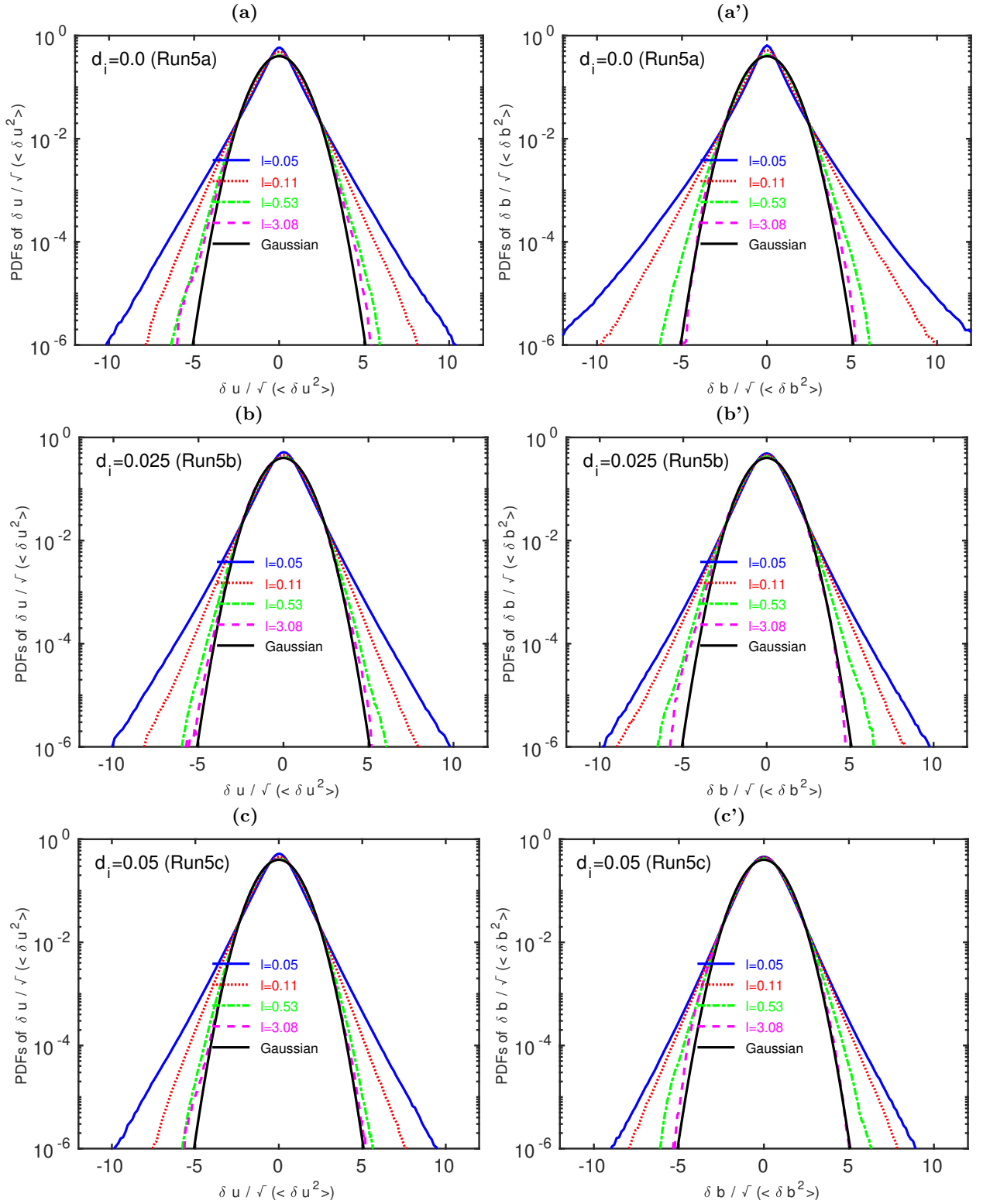


FIG. 7. Semilog (base 10) plots of PDFs of the velocity- (first column) and magnetic-field (second column) increments from *Run5a* (first row), *Run5b* (second row), and *Run5c* (third row) for  $l = 0.05$  (blue solid lines),  $0.11$  (red dotted lines),  $0.53$  (green dashed-dot lines) and  $3.08$  (magenta dashed lines); for reference, we also show zero-mean and unit-variance Gaussian PDFs (black lines).

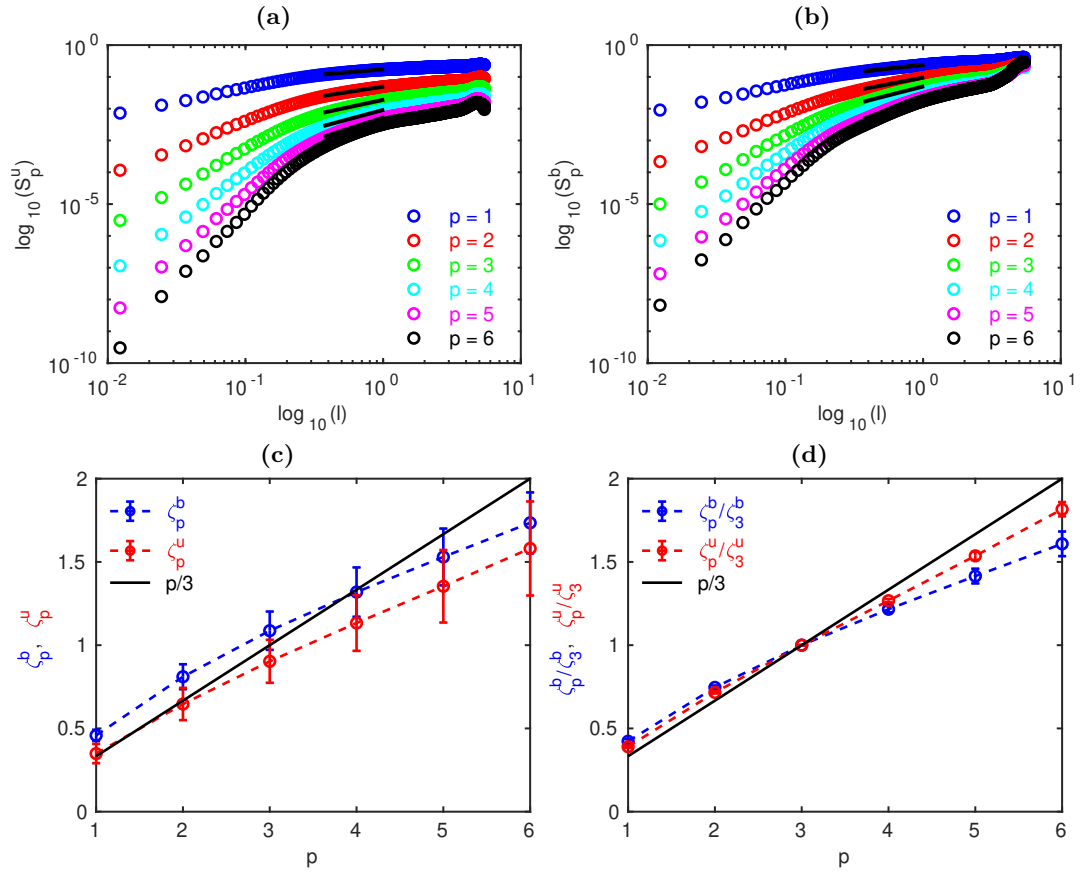


FIG. 8. Log-log (base 10) plots versus  $l$ , at  $t_c$ , for *Run3* and (a) velocity and (b) magnetic structure functions (Eq. 11); the order  $p$  goes from 1 – 6; we indicate by straight, black lines the regions that we use to obtain estimates for the multiscaling exponents (Eqs. 12-13). Plots versus the order  $p$  of (c) the multiscaling exponents (Eqs. 12-13) and (d) their ratios; for reference we show the linear K41 scaling of exponents with  $p/3$ .

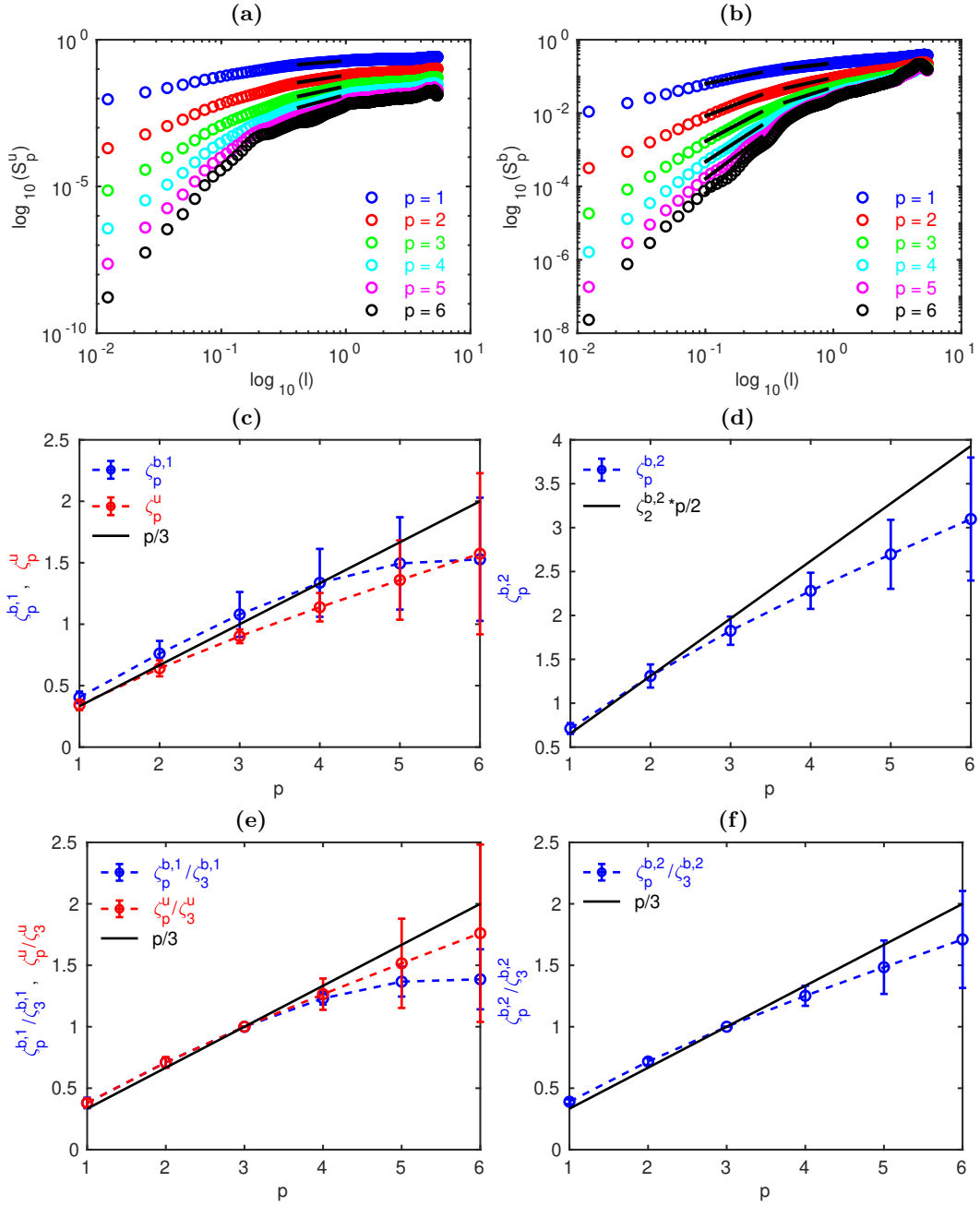


FIG. 9. Log-log (base 10) plots versus  $l$ , at  $t_c$ , for *Run4* and (a) velocity and (b) magnetic structure functions (Eq. 11); the order  $p$  goes from 1 – 6; we indicate by straight, black lines the regions that we use to obtain estimates for the multiscaling exponents (Eqs. 12-13). Plots versus the order  $p$  of the multiscaling exponents (Eqs. 12-13) for (c) the inertial range and (d) the intermediate-dissipation range. Plots versus the order  $p$  of the ratios of multiscaling exponents (Eqs. 12-13) for (e) the inertial range and (f) the intermediate-dissipation range; for reference we show simple scaling predictions.

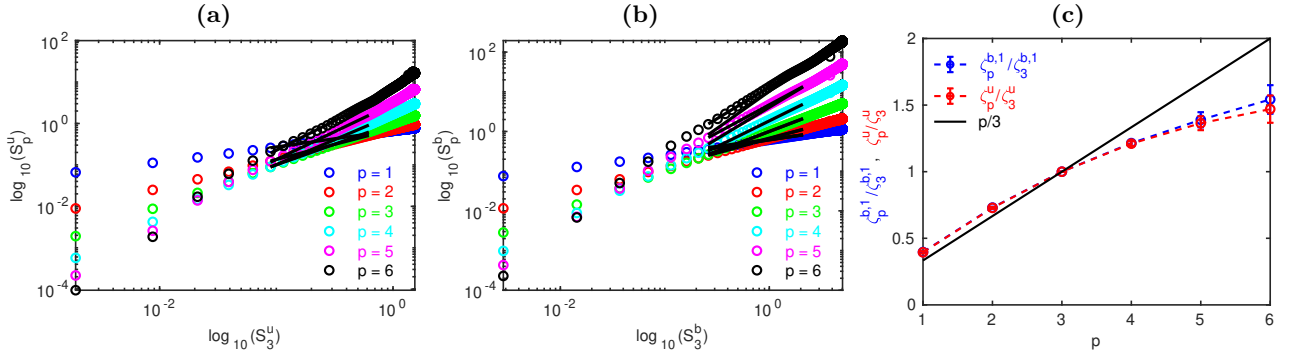


FIG. 10. Log-log (base 10) ESS plots (see text), at  $t_c$ , for *Run5a* and (a) velocity and (b) magnetic structure functions (Eq. 11); the order  $p$  goes from 1 – 6; we indicate by straight, black lines the regions that we use to obtain estimates for the ratios of multiscaling exponents (Eqs. 12-13). Plots versus the order  $p$  of (c) the ratios of multiscaling exponents (Eqs. 12-13); for reference we show the K41 scaling of exponents with  $p/3$ .

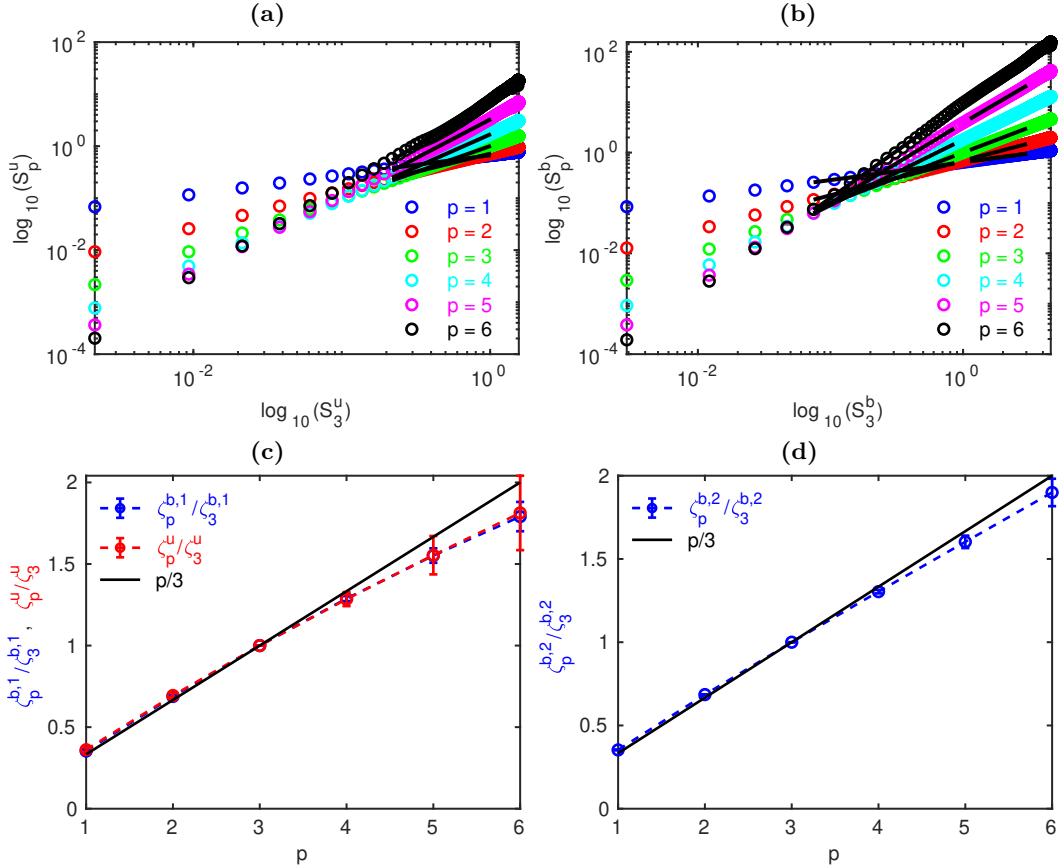


FIG. 11. Log-log (base 10) ESS plots (see text), at  $t_c$ , for *Run5b* and (a) velocity and (b) magnetic structure functions (Eq. 11); the order  $p$  goes from 1 – 6; we indicate by straight, black lines the regions that we use to obtain estimates for the ratios of multiscaling exponents (Eqs. 12-13). Plots versus the order  $p$  of the ratios of multiscaling exponents (Eqs. 12-13) for (c) the inertial range and (d) the intermediate-dissipation range; for reference we show the K41 scaling of exponents with  $p/3$ .

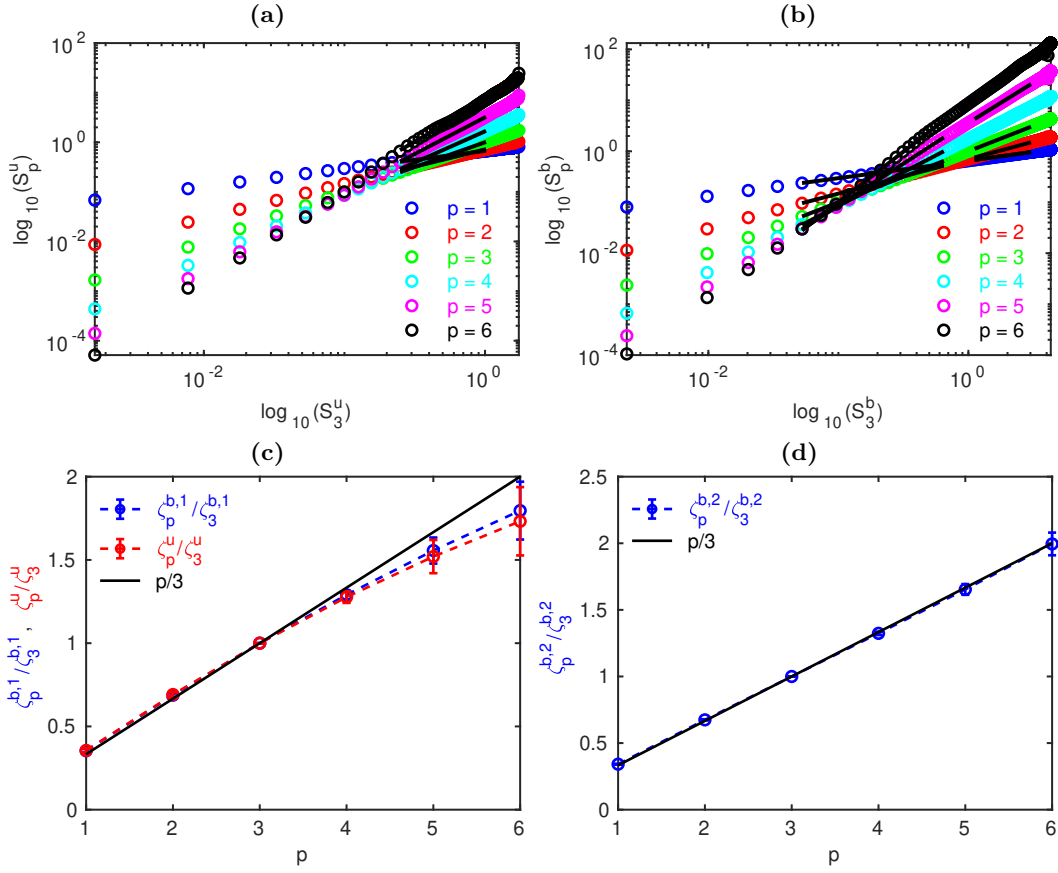


FIG. 12. Log-log (base 10) ESS plots (see text), at  $t_c$ , for *Run5c* and (a) velocity and (b) magnetic structure functions (Eq. 11); the order  $p$  goes from 1 – 6; we indicate by straight, black lines the regions that we use to obtain estimates for the ratios of multiscaling exponents (Eqs. 12-13). Plots versus the order  $p$  of the ratios of multiscaling exponents (Eqs. 12-13) for (c) the inertial range and (d) the intermediate-dissipation range; for reference we show the K41 scaling of exponents with  $p/3$ .

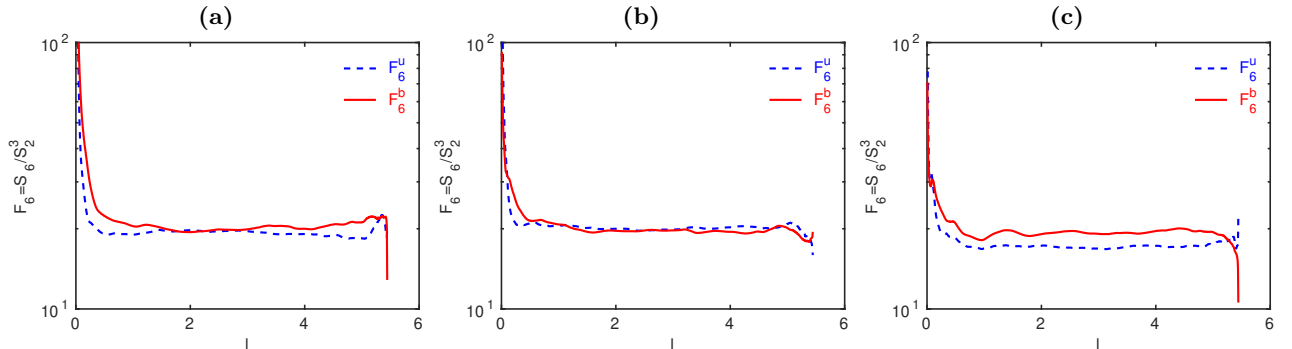


FIG. 13. Semilog plots of the hyperflatnesses (Eq. 14), for the velocity and the magnetic fields, in (a) *Run5a*, (b) *Run5b*, and (c) *Run5c*.

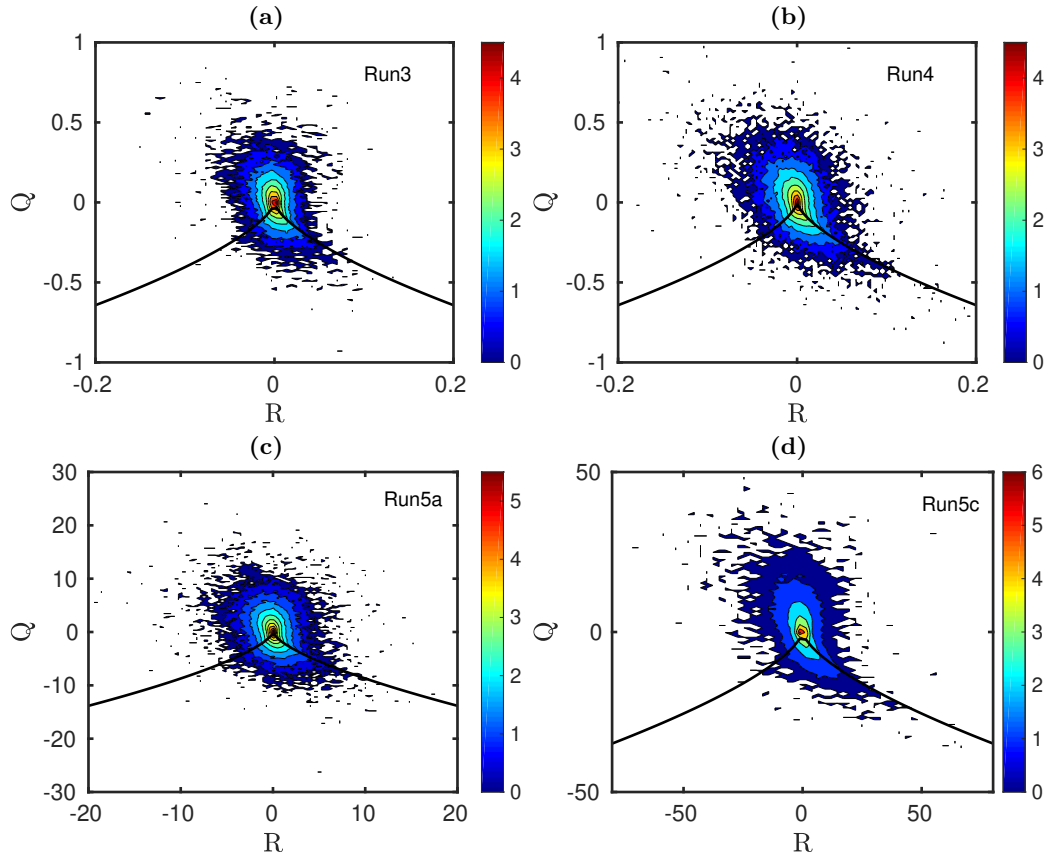


FIG. 14. Color-contour plots of the JPDFs of  $Q$  and  $R$  for (a) *Run3*, (b) *Run4*, (c) *Run5a*, and (d) *Run5c*.

